

2D lamellar membrane with nanochannels synthesized by bottom-up assembly approach for the superior photocatalytic hydrogen evolution

Weiming Zhou^a, Yiting Wu^a, Hongqiang Huang^a, Mingxin Zhang^a, Xuhui Sun^b, Zequn Wang^b, Fei Zhao^d, Houyu zhang^d, Tengfeng Xie^e, Meng An^{b,***}, Liwei Wang^{c,**}, Zhanhui Yuan^{a,*}

^a College of Materials Engineering, Fujian Agriculture and Forestry University, Fuzhou, 350002, China

^b College of Mechanical and Electrical Engineering, Shaanxi University of Science and Technology, Xi'an, 710021, China

^c College of Materials and Chemical Engineering, Minjiang University, Fuzhou, 350108, China

^d State Key Laboratory of Supramolecular Structure and Materials, Jilin University, Changchun, 130012, China

^e Institute of Physical Chemistry, College of Chemistry, Jilin University, Changchun, 130012, China

ARTICLE INFO

Keywords:

2D lamellar membrane
Nanochannels
BiOCl
Photocatalyst
Hydrogen evolution

ABSTRACT

Designing nanoscale photocatalysts to improve photocatalytic efficiency is a popular research topic. However, for wide application and friendly environment, achieving good dispersion and multiple recycling of photocatalysts at the nanoscale remains challenging. Herein, a general bottom-up assembly method is proposed for designing a class of two-dimensional lamellar membranes (2DLMs) for photocatalytic applications. A bismuth oxychloride (BiOCl) nanosheet (BN) was used as a demo photocatalyst to construct a 2DLM via self-stacking. The designed BiOCl membrane (BM) exhibited excellent physical properties including flexibility, mechanical strength (tensile strength = 15.75 MPa, fracture strain = 0.056%), and translucence, as well as superior photocatalytic performance with excellent recycling stability and reusability. The photocatalytic hydrogen evolution performance of BM was 2.5-fold that of BN particles dispersed in an aqueous solution. Further theoretical calculations revealed that a BM with appropriately sized nanochannels can accelerate water transport, and the main horizontal channel size of the BM (3.13 nm) is very close to the size of the ideal water transport nanochannel. Furthermore, the confined internal space reduces the number of hydrogen bonds for water molecules within the nanochannels, thereby enhancing the interfacial reaction rate and photocatalytic efficiency. This study presents a simple bottom-up assembly method to design photocatalysts with further improved performance.

1. Introduction

Photocatalytic technology is considered an effective way to convert solar energy into green fuel and degrade pollutants for environmental remediation. Photocatalytic reactions typically include four main processes, namely, light harvesting, charge separation, charge migration, and surface reactions [1]. Various methods have been widely applied to improve the efficiency of the above four processes, such as adjusting the particle sizes, loading cocatalysts, and constructing heterojunctions [2], thereby improving the efficiency of the photocatalysts. Most contemporary, photocatalysts exist as nanomaterials, and scientists are constantly pursuing smaller photocatalyst particles. Increasing the specific surface area can expose active sites by reducing the particle size of

the photocatalyst, improving the surface reaction rate [3]. However, it will be limited by the quantum confinement effect of size, thus increasing the bandgap and affecting the photocatalytic efficiency [4]. Moreover, in practical applications, nanoscale photocatalysts in a solution are difficult to disperse, recover and reuse, thereby causing environmental pollution [5]. Therefore, finding a way that can not only improve the photocatalytic efficiency but also solve the issues caused by nanoscale photocatalyst it will be a welcomed development.

Contemporary nanomaterials can be divided into three categories based on the number of dimensions, including zero-dimensional (0D) quantum dots/nanoparticles, one-dimensional (1D) nanofibers/nanowires/nanorods/nanotubes, and two-dimensional (2D) nanoplates/nanosheets [6,7]. All these nanomaterials with different dimensions

* Corresponding author. College of Materials Engineering, Fujian Agriculture and Forestry University, Fuzhou, 350002, China.

** Corresponding author.

*** Corresponding author.

E-mail addresses: anmeng@sust.edu.cn (M. An), wlw@mju.edu.cn (L. Wang), zhanhuiyuan@fafu.edu.cn (Z. Yuan).

<https://doi.org/10.1016/j.rser.2022.112767>

Received 17 March 2022; Received in revised form 13 June 2022; Accepted 3 July 2022

Available online 13 July 2022

1364-0321/© 2022 Elsevier Ltd. All rights reserved.

exhibit unique properties owing to their different size effects. For example, 0D nanomaterials have the largest specific area and adjustable electronic and optical properties but agglomerate easily, whereas 1D nanomaterials are favorable for the rapid long-distance transmission of photogenerated electrons along the longitudinal dimension of nanocrystals [8–10]. 2D photocatalytic nanomaterials, including metal oxides [11], graphitic carbon nitride (g-C₃N₄) [12], black phosphorus (BP) [13], transition metal carbides/nitrides (MXenes) [14], transition metal dichalcogenides [15], metal-organic framework (MOF) [16], etc., have attracted significant research interest owing to their large specific area, high density of exposed active sites and unusual surface chemistry properties [17]. In recent years, based on polymers, biopolymers, minerals and other matrix materials, nanomaterials have been constructed into membrane [18,19] or film materials [20,21] via methods such as electrostatic spinning [22], vacuum filtration [18], electrospray [23], and solution casting [24], to achieve the functional combination of nanomaterials on the membrane and solve the issues of nanoscale photocatalysts. In addition, a lamellar membrane as a 2D materials can be self-assembled by stacking nanosheets under van der Waals (vdW) forces, hydrogen bonding, π - π interactions, and so on [25], which contain interlayer capillaries (horizontal channels) formed between neighboring nanosheets and gaps (vertical channels) formed between the edges of the nanosheets [26,27]. These nanochannels interconnect to form numerous fluid transport pathways. To enter the nanochannels, the fluids are converted from the bulk to a nanofluid as they pass through the nanochannel [28]. In contrast, the transport behavior of fluids in nanochannels is significantly different from that at the macroscale [29]. Compared with bulk water, the speed of water flowing through the nanochannels is significantly higher. Geim et al. first found that the nanocapillary networks within a graphene oxide (GO) lamellar membrane were filled with monolayer water under ambient conditions, while the capillary-like pressure provided sufficient flow to allow unimpeded permeation of water [30]. Furthermore, molecular dynamics (MD) simulations were conducted to study the water transport behavior of the 2D nanochannels. Chen et al. investigated the mechanism of water transport in 2D nanochannels and evaluated the interfacial interactions between water molecules and GO using MD simulations. The results showed that the water flux increased with increase in the interlayer spacing, and there was an optimal interlayer spacing for the interfacial interaction between water molecules and GO [31]. Moreover, the interlayer spacing of the lamellar membrane exhibited excellent adjustability [32]. To date, various methods have been adopted to regulate the interlayer spacing of lamellar membranes, including surface modification of 2D materials [33], intercalation of molecules or nanomaterials [34,35], and construction of heterojunction [36].

In addition, the high surface-to-volume ratio of nanochannels in the lamellar membrane provides a larger contact area for the fluid [37], while the interlayer spacing significantly influences the surface-to-volume ratio of nanochannels, and the length of nanochannel extends the distance and time for chemical reactions. Raidongia et al. studied the effects of the interlayer spacing and length of the nanochannel on chemical reactions, and the results showed that the reaction rate increased with decrease in the channel interlayer spacing and increase in the channel length [38]. Similarly, 2D nanochannels have been used in applications such as lithium-ion batteries [39] and supercapacitors [40] because of their large contact area and accelerated fluid transport. In addition, the characteristics of the water in the nanochannels are different from those in the bulk phase. Owing to the nanochannel confinement, the number of hydrogen bonds with adjacent water molecules is usually lower than that in the bulk phase [29,41], which changes the hydrogen bonding state of water molecules and makes it easier for them to escape [42]. Therefore, lamellar membranes with nanochannels constructed using 2D materials have the advantages of ultra-fast water transfer, high surface-to-volume ratio, and confined water with weak hydrogen bonds, providing unprecedented possibilities for increasing photocatalytic performance by promoting the surface

reaction rate. However, there have been no relevant reports of nano photocatalysts designed as two-dimensional lamellar membranes (2DLMs) for photocatalytic hydrogen evolution (PHE). The lamellar membrane also has excellent structural stability and flexibility [43], which would endow it wide application and scope good recycling.

Bismuth oxychloride (BiOCl) is a typical 2D metal oxide photocatalyst with a unique layered crystal structure comprising alternating [Bi₂O₂]²⁺ layers and Cl⁻ slabs. It generates an internal electric field perpendicular to the alternating layer, promoting the directional movement of photogenerated electrons and holes [44]. Over the past few years, BiOCl has been extensively explored in a variety of photocatalytic applications including water splitting [45], pollutant removal [46], carbon dioxide reduction [47], nitrogen fixation [48], and so on [49,50]. As a typical 2D nanomaterial, BiOCl has been used as a functional material to prepare composite membranes with other substrates for evaporation [51], decontamination [52], and separation [53]. However, the photocatalytic performance of these membranes is affected by the substrates used, such as polymers and cellulose.

In this study, a traditional BiOCl nanosheet (BN) synthesized as a demo photocatalyst was used to construct a 2DLM by vacuum filtration. The resultant showed that BiOCl membrane (BM) self-assembled layer-by-layer by BN to form a directional arrangement structure, that contains abundant nanochannels (main horizontal channel size 3.13 nm) and possesses good flexibility and mechanical strength. MD simulations and finite element analysis were also used to confirm that a reasonable design of 2DLM with a specific size of nanochannels was advantageous for ultrafast transport of water within the nanochannels. Moreover, the number of hydrogen bonds exhibited by a confined water molecule within the nanochannels is lower than that in the bulk phase, which makes it easier for water molecules to get rid of the other water molecules and increases the probability of collision with the photocatalyst. Benefiting from the synergy of rapid mass transfer and confined water, the interface reaction between the photocatalyst and water is improved, so the PHE performance of BM is 2.5-fold that of individually dispersed BN particles in an aqueous solution. 2DLM constructed by nano photocatalyst shows further superior photocatalytic performance and advantages in terms of recovery, reuse, and wider application. In addition, the preparation method is simple, inexpensive, and easily scalable. The strategy of designing a BM with nanochannels to improve photocatalytic performance under rapid mass transfer and confined water can be potentially reflected and extended to all nano photocatalysts.

2. Experimental section

2.1. Materials

All the chemical reagents were of analytical grade and used without further purification. Bismuth nitrate (Bi(NO₃)₃·5H₂O), sodium chloride (NaCl), polyvinylpyrrolidone (K30, PVP) and D-mannitol were purchased from Sinopharm Chemical Reagent Co., Ltd, China.

2.2. Samples preparation

BN was synthesized according to the hydrothermal methods proposed in previous studies [54,55]. Bi(NO₃)₃·5H₂O (1 mmol) and PVP (0.400 g) were dissolved in 25 mL of a D-mannitol solution (0.1 mol/L) and stirred vigorously for 10 min. Then, 5 mL of a saturated NaCl solution was slowly added to the above mixture to obtain a uniform white suspension. After stirring for another 10 min, the mixture was transferred to a 45 mL Teflon-lined stainless-steel autoclave, was heated at 160 °C for 3 h, and then was cooled naturally to room temperature. The solid powder collected by centrifugation and washed six times with deionized water to remove residual ions. The final products were obtained via freeze-drying.

BM was prepared by thoroughly stirring 30 mg BN particles and 7 mL deionized water for 10 min to form a suspension, followed by ultrasound

for 45 min, this was repeated at least five times. Subsequently, upon vacuum assistance, the resulting BN suspension was slowly filtered through a porous substrate (Celgard 3501, 0.22 μm pore size, Celgard, USA) to form a membrane with a diameter of 3.8 cm. Finally, the BM was obtained by naturally drying and removing from the substrate.

2.3. Characterization

The crystal structures of the as-prepared samples were determined using X-ray diffraction (XRD) on a diffractometer (Ultima IV, Rigaku, Japan) with Cu-K α radiation ($\lambda = 1.5418 \text{ \AA}$) at 40 kV and 40 mA. The tensile test was carried out using a universal testing machine (Instron 3342, Instron, USA) at 25 $^{\circ}\text{C}$, and the samples were tailored to a width of 1 cm and a length of 3 cm. The morphology was studied using field emission scanning electron microscopy (FE-SEM, Regulus 8100, Hitachi, Japan) with 5.00 kV scanning voltage and transmission electron microscopy (TEM, FEI Talos F200 \times G2, Thermo Fisher, USA). UV-Vis DRS was recorded on a UV-vis spectrophotometer (UV-2600, Shimadzu, Japan) with BaSO $_4$ as a reference. The transient photocurrent response was measured using an electrochemical workstation (CS310H, Corrtest, China) with a 300 W xenon lamp (FX300), a platinum plate, and Ag/AgCl (saturated KCl) (SCE) as the counter electrode and reference electrode, respectively. The surface areas and pore sizes were determined using analyzer (BELSORP-mini II, Microtrac BEL, Japan) in liquid nitrogen at a temperature (77.3 K). Photoluminescence (PL) spectra were obtained using a fluorescence spectrophotometer (SHIMADZU RF-5301PC, Shimadzu, Japan) at room temperature. Time-resolved photoluminescence (TRPL) spectra were carried out using transient-steady state fluorescence spectrometer (FLS1000, Edinburgh, UK). Ultraviolet photoelectron spectroscopy (UPS) and valence-band XPS (VB-XPS) was characterized using X-ray photoelectron spectroscopy (ESCALAB250xi, Thermo Fisher, USA). Raman spectra were obtained on a Raman spectrometer (HORIBA HR Evolution, Horiba, Japan) using 532 nm laser excitation.

2.4. Photocatalytic reaction

The PHE experiments were carried out in a closed gas circulation system (Labsolar-6A, Beijing Perfectlight Technology, China) with a 300 W xenon lamp as the light source. Either BM fixed to the scaffold or BN powder was dispersed in 100 mL of an aqueous solution containing 10 mL of triethanolamine (TEOA) in a Pyrex reaction cell (Fig. S1). Before irradiation, the closed gas circulation system was degassed to exorcise internal air. The amount of evolved hydrogen was determined using an online gas chromatograph (GC-7890, TCD, Agilent, USA) where N $_2$ was used as a carrier gas. The recycling stability and reusability were also evaluated by the cycling runs. The reaction was conducted for 60 h, and the aqueous solution was changed every 6 h to ensure the same reaction conditions.

2.5. Molecular dynamics simulation

To study the molecular-level diffusion of water molecules inside nanochannels among the BN, MD simulations were performed using the Large Scale Atomic/Molecular Massively Parallel Simulator (LAMMPS) package [56]. The interatomic interactions in the simulated system were described by the consistent-valence force field (CVFF), and the CVFF parameters were directly obtained from BIOVIA materials studio [57]. The long-range Coulombic force was calculated using the Ewald summation method based on the particle-particle particle-mesh algorithm. The cut-off radius of long-range interactions was 12.5 \AA . To simplify the simulations, only two layers of BN were used to build the nanoscale channel and their dimensional parameters were $10.50 \times 4.28 \times 0.39 \text{ nm}^3$. To explore the effect of nanochannel size on water diffusion, four nanochannels with diameters of 1.47, 2.95, 3.69, and 5.16 nm were modeled, where the numbers of water molecules placed in the

nanochannels were 1000, 2000, 3000, and 4000, respectively. The time step was set as 1.0 fs. The system was relaxed under NPT (500 K, 1 atm) and NVT ensemble with Nose-Hoover thermostat was applied to maintain the system at 500 K. The last simulation time of 3.0 ps was recorded to analyze water diffusion inside the nanoscale channels.

2.6. Finite element method

The transport of water in one nanochannel with capillary force as the driving force was simulated using the finite element method implemented in COMSOL Multiphysics. The liquid motion is governed by the two-phase flow dynamic equation, namely the Cahn-Hilliard equation:

$$\frac{\partial \varphi}{\partial t} + \mathbf{u} \cdot \nabla \varphi = \nabla \cdot \frac{\gamma \lambda}{\varepsilon^2} \nabla \psi \quad (1)$$

$$\psi = -\nabla \cdot \varepsilon^2 \nabla \varphi + (\varphi^2 - 1)\varphi \quad (2)$$

where \mathbf{u} is the fluid velocity (m/s), γ is the mobility ($\text{m}^3 \cdot \text{s} / \text{kg}$), λ is the mixing energy density (N), and ε (m) is the interface thickness parameter. The ψ variable is referred to as the phase field help variable. The following equation relates the mixing energy density and the interface thickness to the surface tension coefficient:

$$\sigma = \frac{2\sqrt{2}\lambda}{3\varepsilon} \quad (3)$$

The multiphysics coupling feature defines the density (kg/m^3) and viscosity (Pa \cdot s) of the mixture to vary smoothly over the interface by using:

$$\rho = \rho_w + (\rho_{air} - \rho_w)V_{f2} \quad (4)$$

$$\mu = \mu_w + (\mu_{air} - \mu_w)V_{f2} \quad (5)$$

where the single-phase water and air properties are denoted as the subscripts of w and air , respectively. V_{f2} is the volume fraction of water. The Navier-Stokes equations describe the transport of mass and momentum for fluids with constant density. The Navier-Stokes equations state:

$$\rho \frac{\partial \mathbf{u}}{\partial t} - \nabla \cdot [-p\mathbf{I} + \mu(\nabla \mathbf{u} + (\nabla \mathbf{u})^T)] + \rho \mathbf{u} \cdot \nabla \mathbf{u} = \mathbf{F}_{st} \quad (6)$$

$$-\nabla \cdot \mathbf{u} = 0 \quad (7)$$

where ρ denotes the density (kg/m^3), μ is the dynamic viscosity (Ns/m^2), p denotes the pressure (Pa). \mathbf{F}_{st} is the surface tension force acting at the air/water interface. To account for the capillary forces, it is crucial to introduce the term of surface tension in the model:

$$\mathbf{F}_{st} = G \nabla \varphi \quad (8)$$

$$G = \lambda \left[-\nabla^2 \varphi + \frac{\varphi(\varphi^2 - 1)}{\varepsilon^2} \right] = \frac{\lambda}{\varepsilon^2} \psi \quad (9)$$

where φ is the phase field parameter, and G is the chemical potential (J/m^3).

3. Results and discussion

3.1. Characterization of BN and BM

The fabrication process of BM is shown in Fig. 1(a). The BN particles were evenly dispersed in water under ultrasonication to obtain a BN suspension solution, and then BM was formed by vacuum filtration. The crystallinity and phase purity of BN and BM were confirmed by XRD analysis, as shown in Fig. 1(b), and the tetragonal phase of BiOCl with lattice parameters of $a = 0.3891 \text{ nm}$ and $c = 0.7369 \text{ nm}$ (JCPDS No. 00-0066-0249) was well indexed. The (001) peak intensity of BM is much

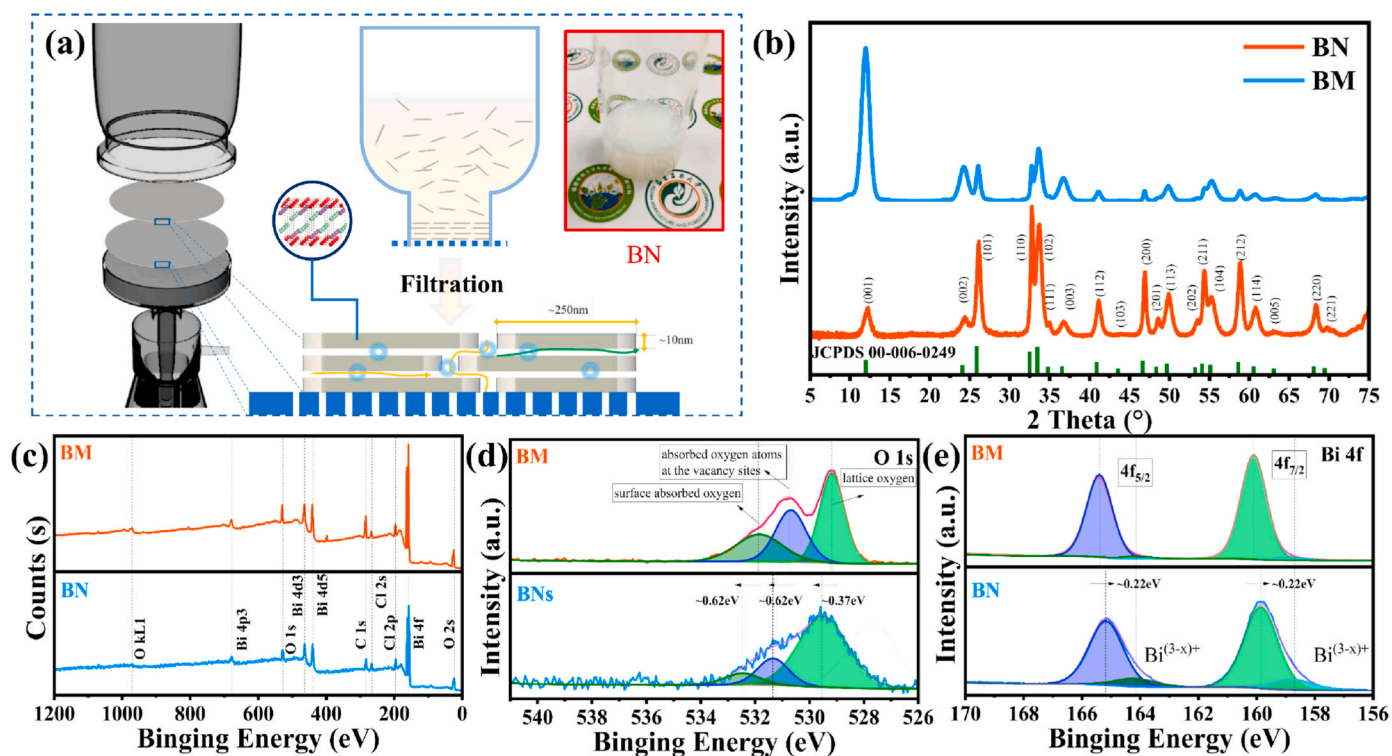


Fig. 1. Preparation and characterization of BN and BM. (a) The fabrication process of BM. (b) XRD pattern, (c) XPS spectra, high-resolution XPS spectra of (d) O1s and (e) Bi 2f of BN and BM.

higher than that of BN, indicating the ordered stacking of BN into BM, while the BN powder exhibits a disordered arrangement [58].

The X-ray photoelectron spectroscopy (XPS) survey spectra and high-resolution XPS spectra of O 1s, Bi 2f, Cl 2p, and C 1s of BN and BM are shown in Fig. 1(c–e) and Fig. S2, respectively. As evident from the XPS survey spectra, Bi, Cl, O and C elements were present in both BN and BM (Fig. 1(c)). The high-resolution XPS spectra of BN shows three peaks located at 529.6, 531.4, and 532.5 eV (Fig. 1(d)) in the O 1s spectrum corresponding to lattice oxygen, absorbed oxygen atoms at the vacancy sites, and surface absorbed oxygen, respectively [59]. Moreover, the two additional peaks (158.7 and 164.1 eV) of the low binding energy result from the partial reduction of Bi^{3+} to $\text{Bi}^{(3-x)+}$ by the oxygen vacancy [60] (Fig. 1(e)). In the spectra of BM, the O 1s peak shifted to a lower binding energy, while the peaks of Bi^{3+} 4f_{5/2} and 4f_{7/2} at 160.1 and 165.4 eV exhibit a slight blue-shifting and a significantly reduction in the intensity of the two additional peaks compared with BN, indicating that

the oxygen vacancy concentration is reduced during the self-stacking [47].

The free-standing BM can be easily detached from the porous substrate and its digital photographs are shown in Fig. 2(a and b). The BM could be easily folded without breakage (Fig. 2(a)), showing good flexibility. As shown in Fig. 2(b) and Fig. S3, the slightly yellowish membrane is also translucent. To determine the stability of the BM in an aqueous solution, the BM was immersed in either water or TEOA (10 vol%) aqueous solution, as shown in Fig. 2(c). BM remained intact without any loosening after six days of immersion in either water or TEOA aqueous solution, showing good stability [43]. As shown in Fig. 2(d), the BM exhibited a tensile strength of 15.75 MPa and a fracture strain of 0.056%. Moreover, the inset of Fig. 2(d) shows that the free-standing BM (1 cm width and 6.46 μm thick) can lift a weight of 20 g, which is mechanically robust. The interlayer forces of the lamellar membrane play an important role in maintaining its structure and

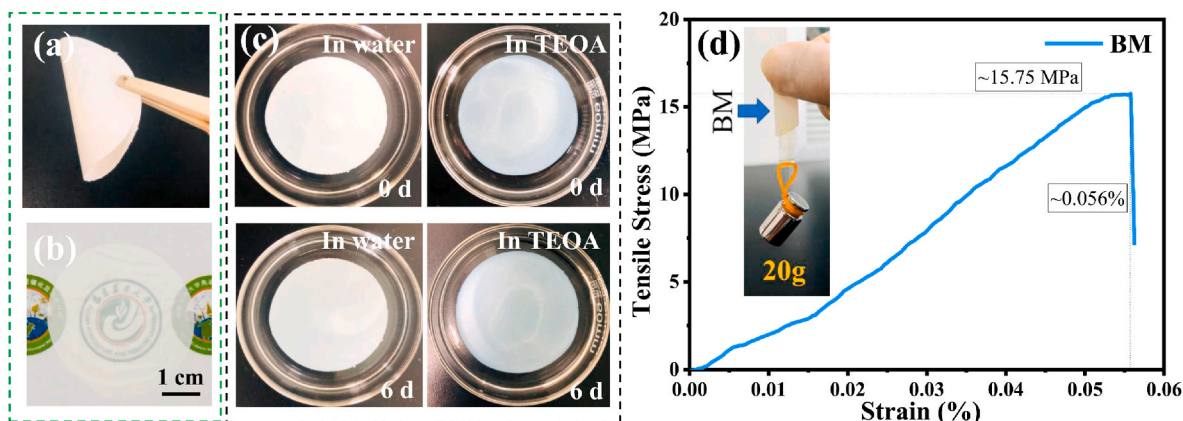


Fig. 2. Digital photograph of (a) folded and (b) unfolded of BM. (c) Immersed in water or TEOA for 0 day and 6 days of BM. (d) Typical stress-strain curves of BM (inset: the photograph of BM holds 20 g counterweight).

mechanical strength. Compared to the BN sample, the $-\text{OH}$ stretching band of BM is shifted to a lower wavenumber and the matching deformation band is slightly shifted to a higher wavenumber (Fig. S4), confirming the formation of hydrogen bonds between the BiOCl nanosheets [60,61] and endowing BM with good mechanical strength and stability. Their excellent physical properties, including good flexibility, mechanical strength, and translucency, are suitable for a wide range of applications.

Fig. 3(a-f) shows the morphology of BN and BM. Most BiOCl exhibit a square shape with a diameter of approximately 250 nm (Fig. 3(a and b)). BM comprises a BN arranged layer-by-layer in an orderly manner with vertical channels between the edges of the BN (Fig. 3(c)) and a flat membrane surface (Fig. 3(d)). The cross-sectional SEM images of BM in Fig. 3(e and f) shows that the lamellar membrane was assembled by the directional stacking of BN with thickness of approximately 6.46 μm (Figs. S5(a and b)), and exhibits successive 2D nanochannels. The top view HRTEM images of BN shows a lattice spacing of 0.27 nm corresponding to the (110) atomic plane, where O atoms are densely arranged perpendicular to the (001) surface (Fig. 3(g, i)). The side view HRTEM images of BN show a lattice spacing of 0.74 nm corresponding to the atomic stacking of $[\text{Bi}_2\text{O}_2]^{2+}$ slabs (Fig. 3(h, j)) [62]. Moreover, the thickness of the BN is about 10.7 nm (Figs. S5(c and d)), which is approximately 15 times thicker than a BiOCl monolayers [63].

3.2. Optical and photoelectrochemical properties

The optical and photoelectrochemical properties of semiconductors significantly influence their photocatalytic performance. UV-vis DRS spectra were used to study the photo-absorption properties of BN and BM, as shown in Fig. 4(a) and Fig. S6(a), revealing that the photo-absorption curves of BN and BM are similar. The band gap energy (E_g) near the optical absorption edge was obtained from tangent lines to the curve of the square root of the Kubelka-Munck (K-M) function *versus* absorbed light energy [64]. In Fig. 4(b) and Fig. S6(b), BN and BM are similar in term of E_g (3.32 eV) [55]. However, samples with E_g larger than 3.10 eV (400 nm) can effectively absorb ultraviolet light but not visible light. Furthermore, to determine the influence on the E_g by

changing the number of BiOCl layers caused by the self-stacking of BN, the E_g values with different number of BiOCl layers were calculated using first-principles calculations, and the results show that the E_g are the almost insensitive to the layer numbers (Fig. S7) [65].

The separation and kinetic behavior of the photogenerated electrons and holes in BN and BM were investigated using SPV measurements [66]. Positive signals indicated the migration of photogenerated holes to the surface, whereas negative signals indicated the migration of photogenerated electrons to the surface. The intensity of the SPV signal indicates the separation efficiency of photogenerated electrons and holes. As shown in Fig. 4(c), the SPV signals of BN and BM rarely change, indicating that the separation efficiencies of photogenerated electrons and holes in the two physical arrangements are nearly the same.

Furthermore, a transient photocurrent response was performed to investigate the separation and transfer processes of photogenerated electrons and holes in the liquid [67]. Fig. 4(d) and Fig. S8 shows the photocurrent density curves of the samples under intermittent light irradiation. The photocurrent density of BM increased significantly by approximately 1.9-fold that of BN, which indicates that BM is favorable for the separation and transfer of photogenerated carriers in the liquid. PL and TRPL techniques have been applied to further investigate the recombination behavior of photogenerated carriers (e^- and h^+) [47]. As shown in Fig. 4(e), wherein the PL spectra of BN and BM were obtained by excitation at 375 nm, it is obvious that BN shows slightly weaker PL emission intensity than that of BM, indicating a lower photogenerated carrier recombination [68,69]. Furthermore, the PL spectra of BN and BM was deconvoluted into three main emission peaks located at 433.4, 461.1 and 507.1 nm, which are indexed to Cl vacancy, isolated $V_{\text{Bi}}^{\text{III}}$ defects, and triple vacancy associates $V_{\text{Bi}}^{\text{III}}V_{\text{O}}V_{\text{Bi}}^{\text{III}}$, respectively [44]. Notably, the PL intensity of the Cl vacancy and isolated $V_{\text{Bi}}^{\text{III}}$ defects of BN are weaker than that of BM, indicating that it can effectively inhibit photogenerated carrier recombination, which is also verified by the XPS results that show different vacancies for BN and BM. Generally, a shorter average lifetime (τ_{avg}) indicates a faster recombination rate of photogenerated carriers [70]. As shown in Fig. 4(f), the τ_{avg} values of BN and BM were calculated to be 4.29 and 3.03 μs , respectively, which suggests that the photogenerated carriers in BN possess lower recombination

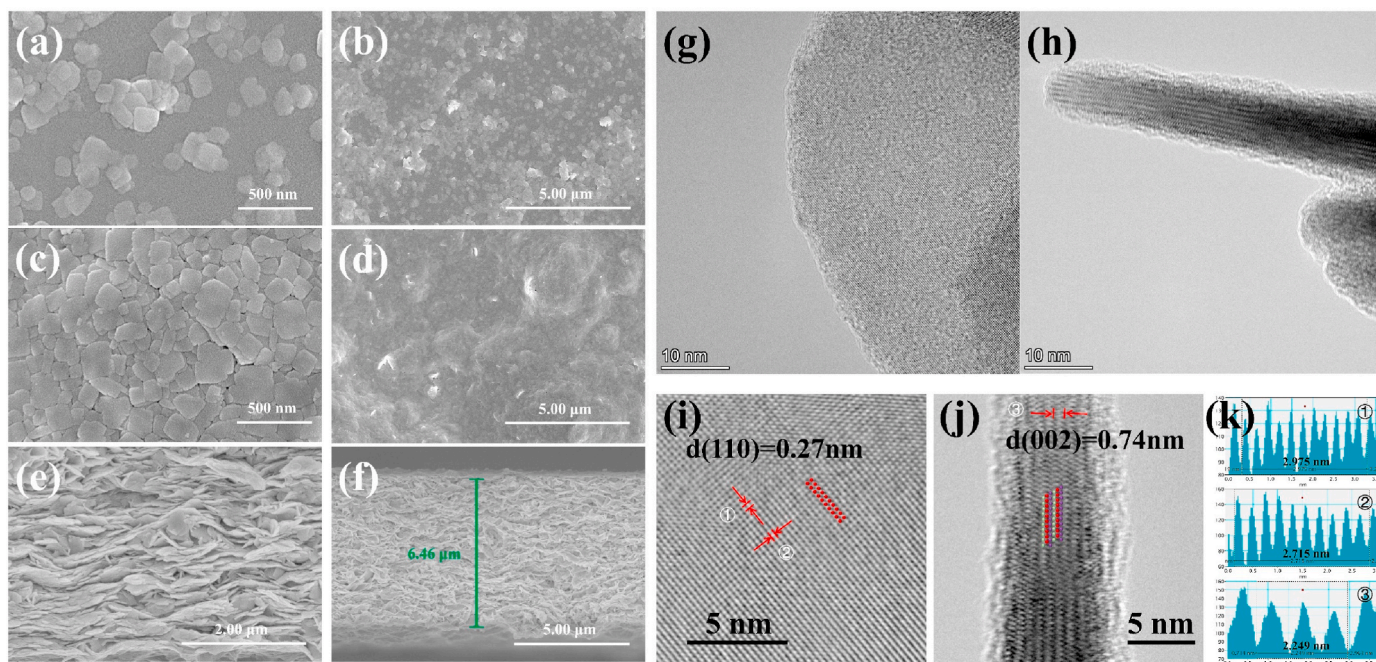


Fig. 3. SEM images of (a, b) BN and (c, d) BM. (e, f) cross-sectional SEM images of BM. (g, i) top view and (h, j) side view HRTEM images of BN, (k) intensity profiles in image (i) and (j), respectively. Schematic illustration of BiOCl surface atomic structures is also shown in image (j) (red: O atoms, purple: Bi atoms, reseda: Cl atoms).

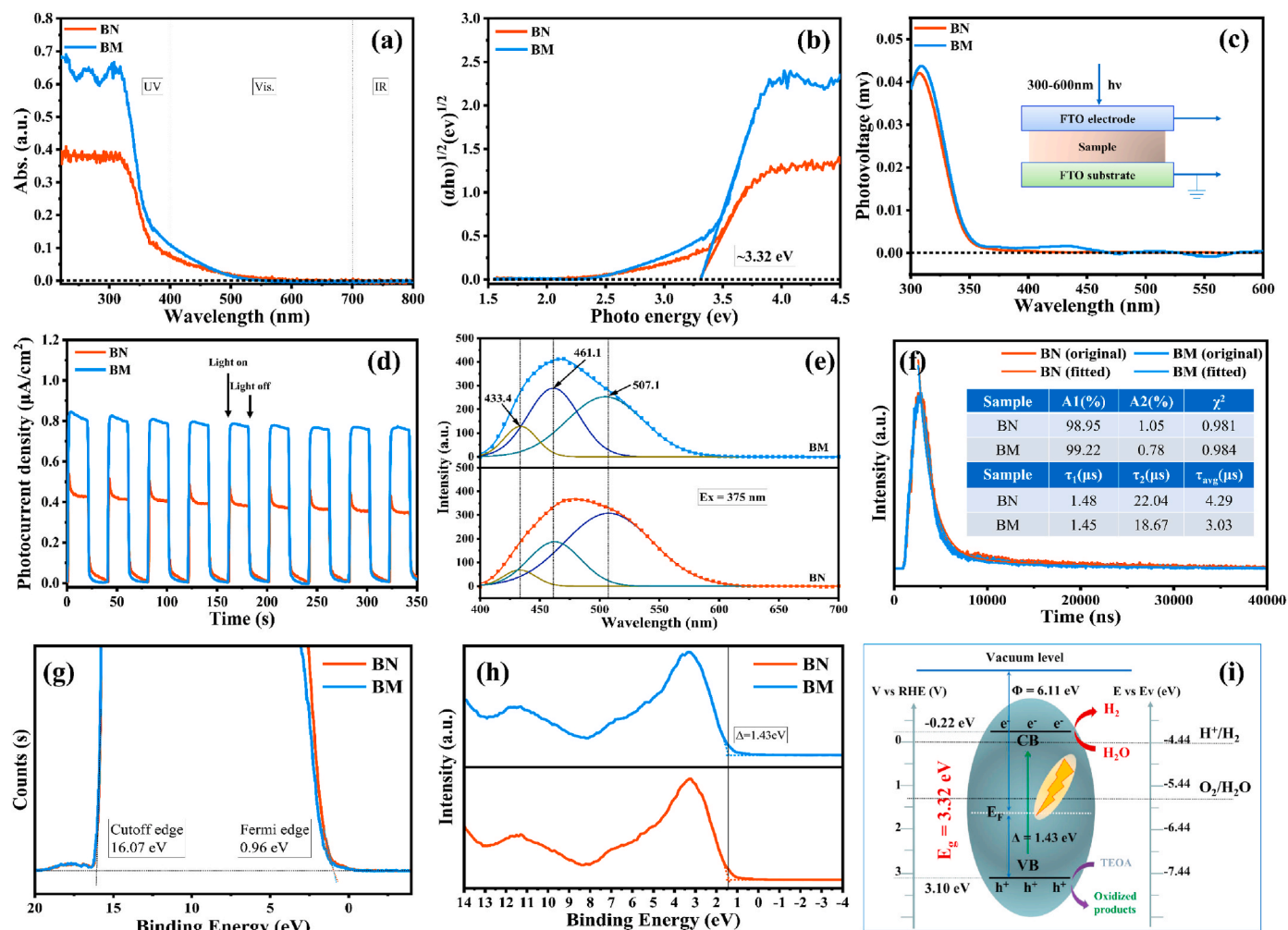


Fig. 4. (a) UV-vis DRS, (b) plots of $(\alpha h\nu)^{1/2}$ vs $h\nu$, (c) SPV signal (inset: the schematic of SPV measurement), (d) transient photocurrent responses, (e) PL spectra, (f) TRPL (g) UPS (h) VB-XPS and (i) the energy band structure and REDOX potentials of BN and BM.

efficiency than BM due to the reduction of vacancies during self-assembly of BiOCl nanosheets into lamellar membranes [47].

Moreover, the energy band structure was investigated using UPS and VB-XPS. The work functions (Φ) of BN and BM were measured and calculated by UPS, in which helium α was used as the ultraviolet light source ($h\nu = 21.22$ eV) [71]. As shown in Fig. 4(e), BN and BM have the same binding energy of Fermi level edge (E_f) and secondary electron cutoff edge (E_c), and the E_f and E_c are 0.96 and 16.07 eV, respectively. The work functions of BN and BM can be estimated using formula $\Phi = h\nu + E_c - E_f$ [72]. The work functions of BN and BM were calculated to be 6.11 eV. The energy difference between the Fermi level (E_f) and vacuum energy level of BN and BM is 6.11 eV. The valence-band maximum (VBM) of BN and BM was further determined using VB-XPS. The results show that the energy difference between the E_f and VBM is 1.43 eV [73]. As a result, the energy level of VBM in BN and BM is determined to be 7.54 eV vs. vacuum level, corresponding to the reversible hydrogen electrode of 3.1 eV [72]. Combined with the E_g and Mott-Schottky plots (Fig. S9), the energy band structure and REDOX potentials of BN and BM are shown in Fig. 4(f). The CB potentials with less than 0 V (vs. NHE) and valence band (VB) potentials with more positive +1.23 V (vs. NHE) of both BN and BM comply with the requirements of potentials for splitting water into hydrogen [74]. In the PHE process, the proton (H^+) of water is reduced to hydrogen (H_2) by the photogenerated electron (e^-) in the CB, while the photogenerated hole (h^+) is trapped by the sacrificial electron donor (TEOA) to prevent the recombination of e^- and h^+ , thus improving the PHE efficiency [75,76].

3.3. Nanochannel sizes and water state

To study the type and size of nanochannel in BM, nitrogen adsorption-desorption isotherms were performed and are shown in Fig. 5(a), where the isotherms curves closely resemble the “type IV” with a type H3 hysteresis loop [74], indicating the formation of slit-like mesopores in the lamellar membrane [77]. The BET specific surface area of BN and BM are 11.367 and 6.495 $m^2 \cdot g^{-1}$, respectively (Fig. S10 (a)).

As shown in Fig. 5(b), the pore size distribution diagram indicates that there are abundant mesopores in the range of 1.9–2.8 nm and 6.3–47.5 nm as horizontal or vertical channels in BM. Meanwhile, the main dimensions of the horizontal channels in the BM were further determined by small angle X-ray scattering (SAXS), as shown in Fig. 5 (c), wherein an intense diffraction peak can be detected at approximately $2\theta = 2.28^\circ$, corresponding to d -spacing of 3.87 nm under Bragg’s law [78]. Furthermore, a small diffraction peak at $2\theta = 9.8^\circ$ is observed, as shown in Fig. 5(d), indicating that the d -spacing is approximately 0.9 nm. The diameters of nanochannels can be estimated by deducting the thickness of $[Bi_2O_2]^{2+}$ slabs (0.74 nm) from the d -spacing to give 3.13 nm and 0.16 nm [58,79].

Moreover, the thickness of the lamellar membranes was accurately controlled by the loading capacity of BN. The XRD pattern, cross-sectional SEM image, and calculated average porosity with different thicknesses of the BM are shown in Figs. S11–S12 and Table S1, respectively, as Supplementary Information, respectively. The results

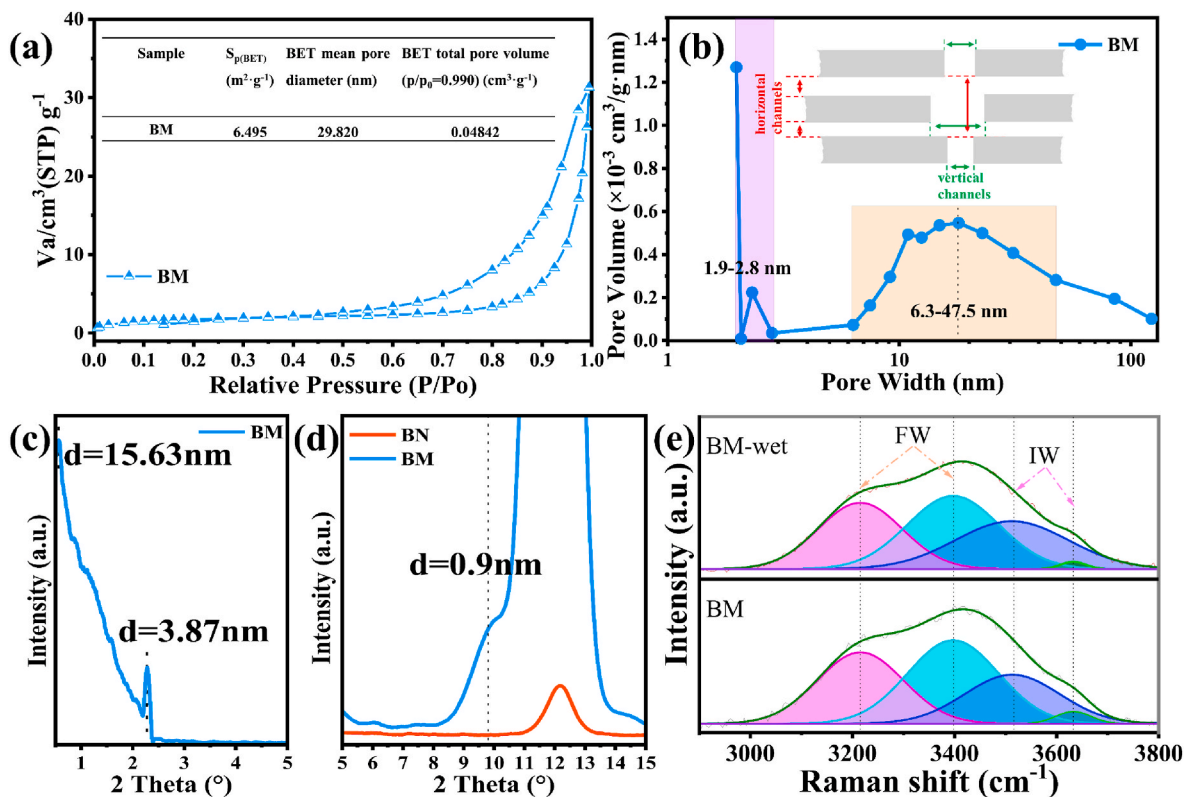


Fig. 5. (a) N_2 adsorption/desorption isotherms, (b) pore size distribution, (c) SAXS pattern and (d) XRD pattern ($2\theta = 5-15^\circ$) of BM. (e) Raman spectra and fitting curves in the energy region of O–H stretching for BM and BM-wet.

showed that the thickness of the BM only slightly influenced the structure of the 2D nanochannel.

In general, water molecules exhibit different characteristics under the confinement of nanochannels compared with those in the bulk phase. Raman spectroscopy was used to confirm the existence of different states of the water molecules [42]. According to the literature, the O–H stretching depends on hydrogen bond, and the stronger the hydrogen bond, the lower the Raman shift [80]. These, O–H stretching peaks are classified into two types of modes, that is, water molecules with four hydrogen bonds (free water (FW), two-proton and two-electron pairs with adjacent water molecules) and weakly or non-hydrogen-bonded water molecules (intermediate water (IW), where the hydrogen bonds of water molecules have been partially or completely broken) [42,81,82]. Raman spectra of BM and BM soaked in deionized water (BM-wet) were fitted through Gaussian function. As shown in Fig. 5(e), the Raman spectrum of BM-wet was deconvoluted into four peaks, corresponding to FW (peaks at 3215 and 3397 cm^{-1}) and IW (peaks at 3512 and 3632 cm^{-1}), respectively [42,81,82]. The peaks of BM at 3512 and 3632 cm^{-1} correspond to the symmetric and asymmetric stretching of weakly hydrogen bonded H_2O molecules [81], respectively, which indicates that the hydrogen bond of IW is enhanced by the effect of –OH on the BiOCl surface. According to Raman spectra, the molar ratio of IW to FW (IW:FW) obtained from BM and BM-wet were calculated to be 0.37 and 0.45, respectively. In contrast, the IW:FW ratio of pure water and BN-wet are only 0.27 and 0.34 (Fig. S13). These results reveal that the number of hydrogen bonds with adjacent confined water molecules in the BM is lower than that in the bulk phase [29,41,83], which changes the hydrogen bonding state of water [32,42].

3.4. MD simulation and finite element analysis

The molecular-level diffusion of water molecules in the BM was studied using MD simulations. There are two types of the nanochannels

with diameter 3.13 and 0.16 nm obtained in the above calculation. One with 0.16 nm is difficult to pass through because the diameter of the water molecule is approximately 0.4 nm. To explore the effect of nanochannel size on water diffusion, nanochannels with diameters 1.47, 2.95, 3.69, and 5.16 nm are modeled. As denoted by the relative density distribution of the water molecules in Fig. 6(a) and Fig. S14, water molecules were evenly distributed in the nanochannels with diameters over 2.95 nm [84]. When the nanochannel diameter is 1.47 nm, there are double layers of water molecules between BN and the relative density near BN is higher because of the hydroxyl group on the surface of BiOCl. Moreover, as the channel diameter increased, the relative density of water molecules decreased owing to the loss of the surface-to-volume ratio within the nanochannels [32]. The radial distribution function (RDF) was calculated to describe the state of the water molecules (Fig. 6 (b) and Fig. S15). It is observed that water molecules in the BM nanochannel with different diameters have similar RDF peaks and $g(r)$ for the first hydration layer increases with the decrease in nanochannel diameter, indicating more densely packed water molecules in the nanochannels [85].

As in the finite element simulation shown in Fig. 6(c and d), the nanochannels made of BN were simplified into a single 2D nanochannel. The length of the single nanochannels was set as $L_n = 50$ nm, and the nanochannel diameter D_n ranged from 1 to 10 nm. As reservoir with $L_r = 10$ nm and $D_r = 20$ nm was used to supply the liquid particles source. The contact angle was set as $\theta = 3\pi/8$ to indicate a hydrophilic surface. The results show that at the entrance of the nanochannel, owing to the capillary force, a large amount of water is sucked into the nanochannel, resulting in a higher velocity. The surface tension provides the pressure difference between the inside and the outside. Interestingly, the pressure difference for different diameters is consistent with our MD simulation results. It is speculated that the pressure difference may also be related to the diffusion coefficient.

Based on the above MD simulation and finite element analysis, it is

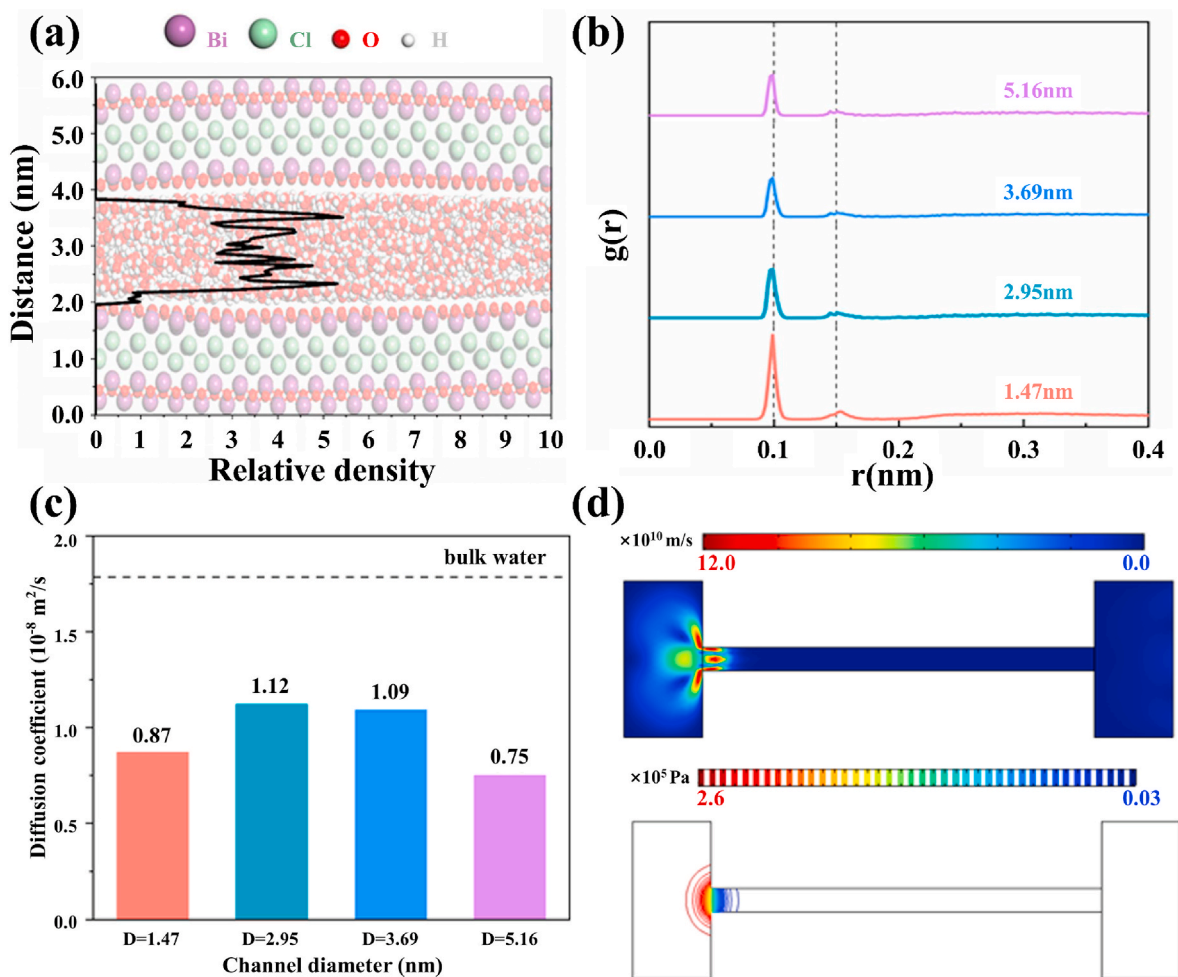


Fig. 6. (a) Relative density distribution of water molecules in the range of 2D nanochannel, where the MD simulation snapshot of channel diameter 2.95 nm is shown as the background. (b) RDF among oxygen atoms of water molecules in the BiOCl nanochannel with different diameters. (c) Diffusion coefficient of water molecular in the nanochannels with different diameters. (d) Mass transfer process induced by capillary force from finite element simulations, where the high velocity corresponds to the entrance of water flow and pressure distribution for channel diameter 2.95 nm.

evident that the capillary force provides the power to promote the rapid transport of water in 2D nanochannels, and the water diffusion coefficient is different for different nanochannel diameters. Consequently, the design and construction of a BM with nanochannels of approximately 3.13 nm are the most ideal for rapid water transport.

3.5. PHE performance and enhancement mechanism

Under the 300 W Xe light source, the PHE performances of BN and BM were conducted as shown in Fig. 7(a). Surprisingly, the PHE performance of BM was 2.5-fold that of BN particles were individually dispersed in aqueous solution containing water and triethanolamine. Furthermore, the apparent quantum yield (AQY) for hydrogen generation by BN and BM were calculated to be 0.195 and 0.76% at 365 nm, respectively (Fig. S16). The recycling stability and reusability of BM were investigated by the cycling PHE experiment, and the results are shown in Fig. 7(b). The PHE performance of the BM remained constant after 10 cycles for 60 h. The XRD spectra of the BM before and after ten PHE cycles are shown in Fig. S17, and there was almost no obvious change in the crystal structure, implying that the BM with 2D nanochannels exhibited outstanding recycling stability and reusability.

As shown above, the self-stacking of BN results in the formation of horizontal and vertical nanochannels, which are interconnected to realize the transfer of water. The MD simulation and finite element analysis also confirmed that the 2DLM with a specific size of

nanochannels is beneficial for the ultra-fast transport of water within nanochannels. Under simulated sunlight irradiation, the photocurrent density of BM increased significantly by approximately 1.9-fold that of BN, which demonstrates that BM is favorable for the separation and transfer of photogenerated carriers in the liquid. Because the nanochannels promote the transfer of the electrolyte, photogenerated carriers have better transfer at the contact interface between BiOCl and the electrolyte and suppress electron-hole recombination. The confining effect of nanochannels on water reduces the number of hydrogen bonds with adjacent water molecules, which allows water molecules to escape from other water molecules and form hydrogen ions. Therefore, the synergistic effect of the nanochannels and confined water increases the collision between the water molecules and BM, thus accelerating the interface reaction between photogenerated electrons and hydrogen ions. As a result, the PHE performance of BM was 2.5-fold that of BN particles were dispersed in aqueous solution. The mechanism of 2DLM enhancing PHE is illustrated in Fig. 7(c).

4. Conclusion

A general bottom-up assembly strategy for the synthesis of BM is described from nanosheets by vacuum filtration. The BM was successfully constructed by self-stacking of BN with a directional arrangement, which possesses abundant horizontal and vertical nanochannels. Compared to BN, BM shows excellent recycling stability, which is

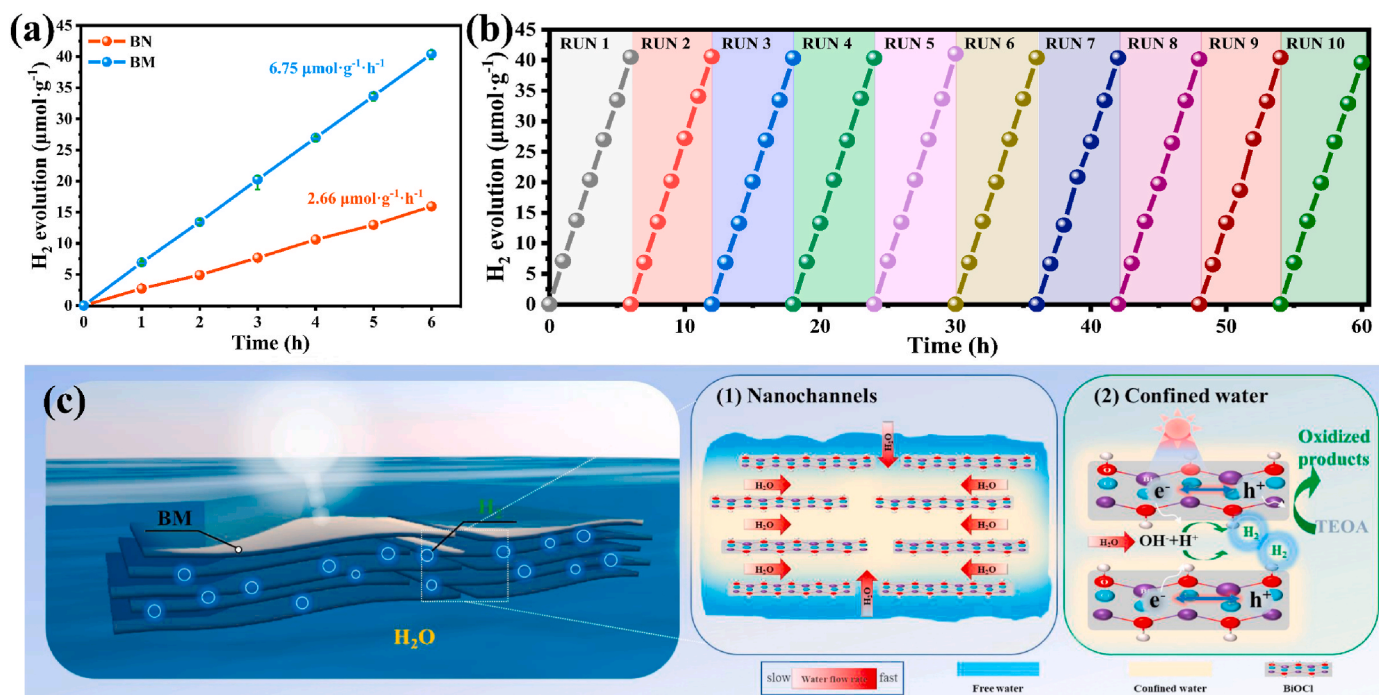


Fig. 7. (a) Photocatalytic H₂ evolution over as-prepared BN and BM under 300 W Xe light (inset: error bars for PHE), (b) cycling tests of BM under the same conditions. (c) Schematic illustration of 2DLM enhancing PHE mechanism.

beneficial for the recovery and reuse of photocatalytic materials. In particular, the PHE performance of the constructed BM was 2.5-fold that of BN particles individually dispersed in aqueous solution owing to the ultra-fast water transport inside nanochannels with a specific size, as revealed by the MD simulation and finite element calculations. In addition, the assembled BM also possesses excellent flexibility, mechanical strength (tensile strength = 15.75 MPa, fracture strain = 0.056%), and even translucency. This contribution sheds light on the bottom-up assembling of 2D lamellar membrane with nanochannels beyond nanosheet photocatalyst, bring in extra consideration, including mass transfer and water states in confined space. This principle can potentially be extended to other types of nanosheets for photocatalysts, enabling the general design of photocatalysts based on 2D lamellar membranes with nanochannels.

Credit author statement

Weiming Zhou: Methodology, Investigation, Formal analysis, Data curation, Writing – original draft, Funding acquisition. **Yiting Wu:** Methodology, Data curation, Conceptualization, Writing – review & editing. **Hongqiang Huang:** Investigation, Data curation. **Mingxin Zhang:** Methodology, Validation, Data curation. **Xuhui Sun:** Methodology, Data curation. **Zequn Wang:** Methodology, Data curation. **Fei Zhao:** Methodology, Data curation. **Houyu zhang:** Resources, Formal analysis. **Tengfeng Xie:** Resources, Formal analysis, Software, Data curation. **Meng An:** Writing – review & editing, Software, Visualization, Supervision, Project administration, Funding acquisition. **Liwei Wang:** Resources, Supervision, Funding acquisition. **Zhanhui Yuan:** Resources, Conceptualization, Supervision, Project administration, Writing – review & editing, Funding acquisition.

Declaration of competing interest

The authors declare that they have no known competing financial interests or personal relationships that could have appeared to influence the work reported in this paper.

Data availability

Data will be made available on request.

Acknowledgements

This work was supported by the Education Research Program for Young and Middle-aged Teachers of Fujian Education Department (No. JAT190132), National Natural Science Foundation of China (No. 52006130), the Youth Innovation Team of Shaanxi Universities (No. 21JP017), the Open Project Program of Key Laboratory of National Forestry & Grassland Bureau for Plant Fiber Functional Materials (Fujian Agriculture and Forestry University) (No. 2019KFJJ15), the Open Project Program of Fujian Key Laboratory of Functional Marine Sensing Materials, Minjiang University (No. MJUKF-FMSM202005), the Natural Science Foundation of Fujian Province (No. 2020J01833), the Open Project Program of Fujian Engineering Research Center of New Chinese lacquer Material (Minjiang University) (No. 323030030702) and the Joint Research Funds of Department of Science and Technology of Shaanxi Province and Northwestern Polytechnical University (No. 2020GXLH-Z-025).

Appendix A. Supplementary data

Supplementary data to this article can be found online at <https://doi.org/10.1016/j.rser.2022.112767>.

References

- [1] Wei Y, Yang N, Huang K, Wan J, You F, Yu R, et al. Steering hollow multishelled structures in photocatalysis: optimizing surface and mass transport. *Adv Mater* 2020;32:2002556.
- [2] Cao S, Piao L, Chen X. Emerging photocatalysts for hydrogen evolution. *Trends Chem* 2020;2:57–70.
- [3] Xu W, Wang J, Yu H, Liu P, Zhang GR, Huang H, et al. Size-dependent electron injection over sensitized semiconductor heterojunctions for enhanced photocatalytic hydrogen production. *Appl Catal, B* 2022;308:121218.
- [4] sKröger J, Jiménez-Solano A, Savasci G, Lau VWh, Duppel V, Moudrakovski I, et al. Morphology control in 2D carbon nitrides: impact of particle size on optoelectronic properties and photocatalysis. *Adv Funct Mater* 2021;31:2102468.

- [5] Qiang Z, Liu X, Li F, Li T, Zhang M, Singh H, et al. Iodine doped Z-scheme $\text{Bi}_2\text{O}_3/\text{CO}_2/\text{Bi}_2\text{WO}_6$ photocatalysts: facile synthesis, efficient visible light photocatalysis, and photocatalytic mechanism. *Chem Eng J* 2021;403:126327.
- [6] Wei Z, Mogan TR, Wang K, Janczarek M, Kowalska E. Morphology-governed performance of multi-dimensional photocatalysts for hydrogen generation. *Energies* 2021;14:7223.
- [7] Daulbayev C, Sultanov F, Bakbolat B, Daulbayev O. 0D, 1D and 2D nanomaterials for visible photoelectrochemical water splitting. A Review. *Int J Hydrogen Energy* 2020;45:33325–42.
- [8] Wang W, Li G, Xia D, An T, Zhao H, Wong PK. Photocatalytic nanomaterials for solar-driven bacterial inactivation: recent progress and challenges. *Environ Sci: Nano* 2017;4:782–99.
- [9] Xu HM, Wang HC, Shen Y, Lin YH, Nan CW. Low-dimensional nanostructured photocatalysts. *J Adv Ceram* 2015;4:159–82.
- [10] Voiry D, Shin HS, Loh KP, Chhowalla M. Low-dimensional catalysts for hydrogen evolution and CO_2 reduction. *Nat Rev Chem* 2018;2.
- [11] Hu S, Qiao P, Zhang L, Jiang B, Gao Y, Hou F, et al. Assembly of TiO_2 ultrathin nanosheets with surface lattice distortion for solar-light-driven photocatalytic hydrogen evolution. *Appl Catal, B* 2018;239:317–23.
- [12] Wang X, Maeda K, Thomas A, Takanabe K, Xin G, Carlsson JM, et al. A metal-free polymeric photocatalyst for hydrogen production from water under visible light. *Nat Mater* 2009;8:76–80.
- [13] Zhu X, Zhang T, Sun Z, Chen H, Guan J, Chen X, et al. Black phosphorus revisited: a missing metal-free elemental photocatalyst for visible light hydrogen evolution. *Adv Mater* 2017;29:1605776.
- [14] Guo Z, Zhou J, Zhu L, Sun Z. MXene: a promising photocatalyst for water splitting. *J Mater Chem* 2016;4:11446–52.
- [15] Lin L, Sherrill P, Liu Y, Lei W, Zhang S, Zhang H, et al. Engineered 2D transition metal dichalcogenides-A vision of viable hydrogen evolution reaction catalysis. *Adv Energy Mater* 2020;10:1903870.
- [16] Li X, Huang Y, Wei WF, Guo WL, Luo Z, Xu J, et al. Metalloporphyrin-anchored 2D MOF nanosheets as highly accessible heterogeneous photocatalysts towards cytochrome c compatible living radical polymerization. *Chem Eng J* 2022;434:134692.
- [17] Li Y, Gao C, Long R, Xiong Y. Photocatalyst design based on two-dimensional materials. *Mater Today Chem* 2019;11:197–216.
- [18] Liu T, Li B, Hao Y, Yao Z. MoO_3 -nanowire membrane and $\text{Bi}_2\text{Mo}_3\text{O}_{12}/\text{MoO}_3$ nano-heterostructural photocatalyst for wastewater treatment. *Chem Eng J* 2014;244:382–90.
- [19] Fatima A, Yasir S, Khan MS, Manan S, Ullah MW, Ul-Islam M. Plant extract-loaded bacterial cellulose composite membrane for potential biomedical applications. *J Bioreour Bioprod* 2021;6:26–32.
- [20] Hsu WP, Mishra M, Liu WS, Su CY, Perng TP. Fabrication of direct Z-scheme $\text{Ta}_3\text{N}_5/\text{WO}_2$ film heterojunction photocatalyst for enhanced hydrogen evolution. *Appl Catal, B* 2017;201:511–7.
- [21] Mbituyimana B, Mao L, Hu S, Ullah MW, Chen K, Fu L, et al. Bacterial cellulose/glycolic acid/glycerol composite membrane as a system to deliver glycolic acid for anti-aging treatment. *J Bioreour Bioprod* 2021;6:129–41.
- [22] Sittirug I-o, Ksapabutr B, Panapoy M. Freestanding hematite nanofiber membrane for visible-light-responsive photocatalyst. *Ceram Int* 2016;42:3864–75.
- [23] Guo J, Yan DYS, Lam FLY, Deka BJ, Lv X, Ng YH, et al. Self-cleaning BiOBr/Ag photocatalytic membrane for membrane regeneration under visible light in membrane distillation. *Chem Eng J* 2019;378:122137.
- [24] Oyeoka HC, Ewulonu CM, Nwuzor IC, Obele CM, Nwabanne JT. Packaging and degradability properties of polyvinyl alcohol/gelatin nanocomposite films filled with water hyacinth cellulose nanocrystals. *J Bioreour Bioprod* 2021;6:168–85.
- [25] Wang S, Yang L, He G, Shi B, Li Y, Wu H, et al. Two-dimensional nanochannel membranes for molecular and ionic separations. *Chem Soc Rev* 2020;49:1071–89.
- [26] Karahan HE, Goh K, Zhang CJ, Yang E, Yildirim C, Chuah CY, et al. MXene materials for designing advanced separation membranes. *Adv Mater* 2020;32:1906697.
- [27] Liu G, Jin W, Xu N. Two-dimensional-material membranes: a new family of high-performance separation membranes. *Angew Chem Int Ed* 2016;55:13384–97.
- [28] Kang Y, Xia Y, Wang H, Zhang X. 2D laminar membranes for selective water and ion transport. *Adv Funct Mater* 2019;29:1902014.
- [29] Tong X, Liu S, Crittenden J, Chen Y. Nanofluidic membranes to address the challenges of salinity gradient power harvesting. *ACS Nano* 2021;15:5838–60.
- [30] Nair RR, Wu HA, Jayaram PN, Grigorieva IV, Geim AK. Unimpeded permeation of water through helium-leak-tight graphene-based membranes. *Science* 2012;335:442–4.
- [31] Li W, Zhang L, Zhang X, Zhang M, Liu T, Chen S. Atomic insight into water and ion transport in 2D interlayer nanochannels of graphene oxide membranes: implication for desalination. *J Membr Sci* 2020;596:117744.
- [32] Zhu H, Hu B, Hu H, He W, Huang J, Li G. Tunable dielectric constant of water confined in graphene oxide nanochannels. *J Mol Liq* 2021;324:115139.
- [33] Wu X, Cui X, Wu W, Wang J, Li Y, Jiang Z. Elucidating ultrafast molecular permeation through well-defined 2D nanochannels of lamellar membranes. *Angew Chem Int Ed Engl* 2019;58:18524–9.
- [34] Wu Y, Xin W, Kong X, Chen J, Qian Y, Sun Y, et al. Enhanced ion transport by graphene oxide/cellulose nanofibers assembled membranes for high-performance osmotic energy harvesting. *Mater Horiz* 2020;7:2702–9.
- [35] Zhang F, Yu L-J, Liu J, Hou L, Li S, Chai H, et al. pH-responsive laminar WSe_2 membrane with photocatalytic antifouling property for ultrafast water transport. *Chem Eng J* 2022;435:135159.
- [36] Wu Y, Fu C, Huang Q, Zhang P, Cui P, Ran J, et al. 2D heterostructured nanofluidic channels for enhanced desalination performance of graphene oxide membranes. *ACS Nano* 2021;15:7586–95.
- [37] Wang J, Chen P, Shi B, Guo W, Jaroniec M, Qiao SZ. A regularly channeled lamellar membrane for unparalleled water and organics permeation. *Angew Chem Int Ed* 2018;57:6814–8.
- [38] Saha K, Deka J, Hens S, Saikia S, Raidongia K. Chemical reactions under the nanofluidic confinement of reconstructed lamellar membranes. *J Mater Chem* 2018;6:22931–9.
- [39] Jin R, Ren C, Kang H, Gao S, Chen S. Stacked Cu_{2-x}Se nanoplates with 2D nanochannels as high performance anode for lithium batteries. *J Colloid Interface Sci* 2021;590:219–25.
- [40] Geng X, Zhang Y, Han Y, Li J, Yang L, Benamara M, et al. Two-dimensional water-coupled metallic MoS_2 with nanochannels for ultrafast supercapacitors. *Nano Lett* 2017;17:1825–32.
- [41] Oh MI, Gupta M, Oh CI, Weaver DF. Understanding the effect of nanoconfinement on the structure of water hydrogen bond networks. *Phys Chem Chem Phys* 2019;21:26237–50.
- [42] Zhu F, Wang L, Demir B, An M, Wu ZL, Yin J, et al. Accelerating solar desalination in brine through ion activated hierarchically porous polyion complex hydrogels. *Mater Horiz* 2020;7:3187–95.
- [43] Wang C, Miao C, Zhu X, Feng X, Hu C, Wei D, et al. Fabrication of stable and flexible nanocomposite membranes comprised of cellulose nanofibers and graphene oxide for nanofluidic ion transport. *ACS Appl Nano Mater* 2019;2:4193–202.
- [44] Zhang Y, Xu Z, Wang Q, Hao W, Zhai X, Fei X, et al. Unveiling the activity origin of ultrathin BiOCl nanosheets for photocatalytic CO_2 reduction. *Appl Catal, B* 2021;299:120679.
- [45] Su T, Shao Q, Qin Z, Guo Z, Wu Z. Role of interfaces in two-dimensional photocatalyst for water splitting. *ACS Catal* 2018;8:2253–76.
- [46] Sharma K, Dutta V, Sharma S, Raizada P, Hosseini-Bandegharai A, Thakur P, et al. Recent advances in enhanced photocatalytic activity of bismuth oxyhalides for efficient photocatalysis of organic pollutants in water: a review. *J Ind Eng Chem* 2019;78:1–20.
- [47] Zhao X, Xia Y, Li H, Wang X, Wei J, Jiao X, et al. Oxygen vacancy dependent photocatalytic CO_2 reduction activity in liquid-exfoliated atomically thin BiOCl nanosheets. *Appl Catal, B* 2021;297:120426.
- [48] Zhao Y, Zhou S, Zhao J, Du Y, Dou SX. Control of photocarrier separation and recombination at bismuth oxyhalide interface for nitrogen fixation. *J Phys Chem Lett* 2020;11:9304–12.
- [49] Li H, Li J, Ai Z, Jia F, Zhang L. Oxygen vacancy-mediated photocatalysis of BiOCl : reactivity, selectivity, and perspectives. *Angew Chem Int Ed Engl* 2018;57:122–38.
- [50] Li J, Li H, Zhan G, Zhang L. Solar water splitting and nitrogen fixation with layered bismuth oxyhalides. *Acc Chem Res* 2017;50:112–21.
- [51] Gao Z, Yang H, Li J, Kang L, Wang L, Wu J, et al. Simultaneous evaporation and decontamination of water on a novel membrane under simulated solar light irradiation. *Appl Catal, B* 2020;267:118695.
- [52] Zhou Q, Huang W, Xu C, Liu X, Yang K, Li D, et al. Novel hierarchical carbon quantum dots-decorated BiOCl nanosheet/carbonized eggshell membrane composites for improved removal of organic contaminants from water via synergistic adsorption and photocatalysis. *Chem Eng J* 2021;420:129582.
- [53] Gao M, Liang H, Bao S, Xu T, Zhang Y, Bai J, et al. Bifunctional $\text{BiOCl}/\text{TiO}_2$ decorated membrane for antibiotic photodegradation and oil-water emulsion separation. *Appl Surf Sci* 2022;578:151960.
- [54] Meili G, Chong X, Jie Z, Shaojuan F, Ran A, Qingmei C, et al. Vacancy associates promoting solar-driven photocatalytic activity of ultrathin bismuth oxychloride nanosheets. *J Am Chem Soc* 2013;135:10411–7.
- [55] Zhang L, Han Z, Wang W, Li X, Su Y, Jiang D, et al. Solar-light-driven pure water splitting with ultrathin BiOCl nanosheets. *Chemistry* 2015;21:18089–94.
- [56] Plimpton S. Fast parallel algorithms for short-range molecular dynamics. *J Comput Phys* 1995;117:1–19.
- [57] Biovia DS. Materials studio. San Diego: Dassault Systemes; 2014., Version 8.
- [58] Ding L, Wei Y, Li L, Zhang T, Wang H, Xue J, et al. MXene molecular sieving membranes for highly efficient gas separation. *Nat Commun* 2018;9:155.
- [59] Wang H, Han Z, Zhou Y, Liu X, Zeng D, Wang W, et al. Efficient photocatalytic chlorine production on bismuth oxychloride in chloride solution. *Appl Catal, B* 2021;297:120436.
- [60] Li H, Chen S, Shang H, Wang X, Yang Z, Ai Z, et al. Surface hydrogen bond network spatially confined BiOCl oxygen vacancy for photocatalysis. *Sci Bull* 2020;65:1916–23.
- [61] Xu H, Liu X, Li H, Zhang L. O_2 activation and $^1\text{O}_2$ generation over phosphate modified BiOCl for efficient photodegradation of organic pollutants. *Appl Catal, B* 2022;314:121520.
- [62] Li H, Shang H, Li Y, Cao X, Yang Z, Ai Z, et al. Interfacial charging-decharging strategy for efficient and selective aerobic NO oxidation on oxygen vacancy. *Environ Sci Technol* 2019;53:6964–71.
- [63] Li J, Zhan G, Yu Y, Zhang L. Superior visible light hydrogen evolution of Janus bilayer junctions via atomic-level charge flow steering. *Nat Commun* 2016;7:11480.
- [64] Paola AD, Cufalo G, Addamo M, Bellardita M, Campostrini R, Ischia M, et al. Photocatalytic activity of nanocrystalline TiO_2 (brookite, rutile and brookite-based) powders prepared by thermohydrolysis of TiCl_4 in aqueous chloride solutions. *Colloids & Surfaces A Physicochemical & Engineering Aspects* 2008;317:366–76.
- [65] Zhang J, Lei SL. Interlayer-decoupled BiOX ($\text{X}=\text{Cl}, \text{Br}, \text{and I}$) sheets for photocatalytic water splitting: a computational study. *Optoelectron Lett* 2021;17:32–5.

- [66] Li Y, Wu Q, Chen Y, Zhang R, Li C, Zhang K, et al. Interface engineering Z-scheme Ti-Fe₂O₃/In₂O₃ photoanode for highly efficient photoelectrochemical water splitting. *Appl Catal, B* 2021;290:120058.
- [67] Fan T, Zhao H, Li G, Zan D, Liu Y, Rong C. Modification with metallic bismuth as efficient strategy for the promotion of photocatalysis: the case of bismuth phosphate. *ChemSusChem* 2016;9:1579–85.
- [68] Li D, Wen C, Huang J, Zhong J, Chen P, Liu H, et al. High-efficiency ultrathin porous phosphorus-doped graphitic carbon nitride nanosheet photocatalyst for energy production and environmental remediation. *Appl Catal, B* 2022;307:121099.
- [69] Liu J, Tao Z, Xie H, Zhang X, Wang H, Xiao H, et al. Facial construction of defected NiO/TiO₂ with Z-scheme charge transfer for enhanced photocatalytic performance. *Catal Today* 2019;335:269–77.
- [70] Yan S, Song H, Li Y, Yang J, Jia X, Wang S, et al. Integrated reduced graphene oxide/polypyrrole hybrid aerogels for simultaneous photocatalytic decontamination and water evaporation. *Appl Catal, B* 2022;301:120820.
- [71] Gao C, Meng Q, Zhao K, Yin H, Wang D, Guo J, et al. Co₃O₄ hexagonal platelets with controllable facets enabling highly efficient visible-light photocatalytic reduction of CO₂. *Adv Mater* 2016;28:6485–90.
- [72] Li Z, Huang F, Xu Y, Yan A, Dong H, Xiong X, et al. Electron-extracting system with enhanced photocatalytic hydrogen production performance: synergistic utilization of Z-scheme and Ohmic heterojunctions. *Chem Eng J* 2022;429:132476.
- [73] Hermans Y, Klein A, Sarker HP, Huda MN, Junge H, Toupance T, et al. Pinning of the fermi level in CuFeO₂ by polaron formation limiting the photovoltage for photochemical water splitting. *Adv Funct Mater* 2020;30:1910432.
- [74] Zhang L, Ran J, Qiao SZ, Jaroniec M. Characterization of semiconductor photocatalysts. *Chem Soc Rev* 2019;48:5184–206.
- [75] Zhang JH, Wei MJ, Wei ZW, Pan M, Su CY. Ultrathin graphitic carbon nitride nanosheets for photocatalytic hydrogen evolution. *ACS Appl Nano Mater* 2020;3:1010–8.
- [76] Cao S, Shen B, Huang Q, Chen Z. Effect of sacrificial agents on the dispersion of metal cocatalysts for photocatalytic hydrogen evolution. *Appl Surf Sci* 2018;442:361–7.
- [77] Kai L, Liang Y, Jian Y, Qiang G, Zhu Y, Liu S, et al. Controllable synthesis of {001} facet dependent foursquare BiOCl nanosheets: a high efficiency photocatalyst for degradation of methyl orange. *J Alloys Compd* 2017;695:238–49.
- [78] Hong S, Zou G, Kim H, Huang D, Wang P, Alshareef HN. Photothermoelectric response of Ti₃C₂T_x MXene confined ion channels. *ACS Nano* 2020;14:9042–9.
- [79] Liu M, Weston PJ, Hurt RH. Controlling nanochannel orientation and dimensions in graphene-based nanofluidic membranes. *Nat Commun* 2021;12:507.
- [80] Liao YY, Picot P, Brubach JB, Roy P, Thill A, Le Caër S. Water adsorption in single- and double-walled inorganic nanotubes. *J Phys Chem C* 2019;123:19768–77.
- [81] Zhao F, Zhou X, Shi Y, Qian X, Alexander M, Zhao X, et al. Highly efficient solar vapour generation via hierarchically nanostructured gels. *Nat Nanotechnol* 2018;13:489–95.
- [82] Sun Q. Raman spectroscopic study of the effects of dissolved NaCl on water structure. *Vib Spectrosc* 2012;62:110–4.
- [83] Park HG, Jung Y. Carbon nanofluidics of rapid water transport for energy applications. *Chem Soc Rev* 2014;43:565–76.
- [84] Qiu R, Yuan S, Xiao J, Chen XD, Selomulya C, Zhang X, et al. Effects of edge functional groups on water transport in graphene oxide membranes. *ACS Appl Mater Interfaces* 2019;11:8483–91.
- [85] Zheng S, Tu Q, Urban JJ, Li S, Mi B. Swelling of graphene oxide membranes in aqueous solution: characterization of interlayer spacing and insight into water transport mechanisms. *ACS Nano* 2017;11:6440–50.